Journal of Materials Chemistry A

Accepted Manuscript

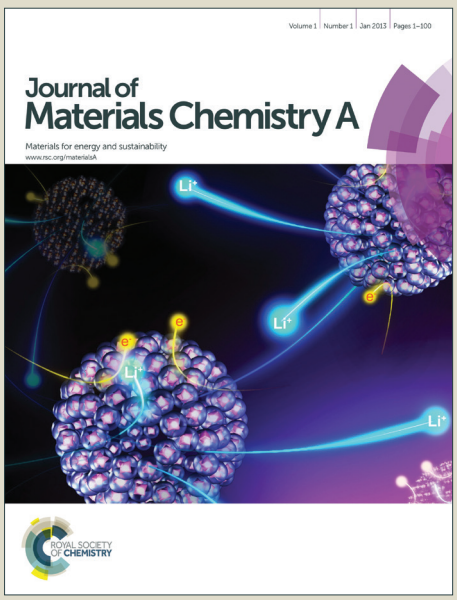

ROYAL SOCIETY OF CHEMISTRY

www.rsc.org/materialsA

Amorphous $Ni(OH)_2$ @ three-dimensional Ni core-shell nanostructures for high capacitance pseudocapacitors and asymmetric supercapacitors

Yuzhi Su[a], Kang Xiao[a], Nan Li[a], Zhao-Qing Liu[a,*], and Shi-Zhang Qiao[b,*]

[a]*School of Chemistry and Chemical Engineering/Guangzhou Key Laboratory for Environmentally Functional Materials and Technology, Guangzhou University, Guangzhou 510006, Guangdong, P.R. China. E-mail: lzqgzu@gzhu.edu.cn (Z.-Q. Liu) Fax: (+86) 20 39366908.*

[b]*School of Chemical Engineering, University of Adelaide, Adelaide, SA5005, Australia. E-mail: s.qiao@adelaide.edu.au. (S.-Z. Qiao)*

TABLE OF CONTENTS:

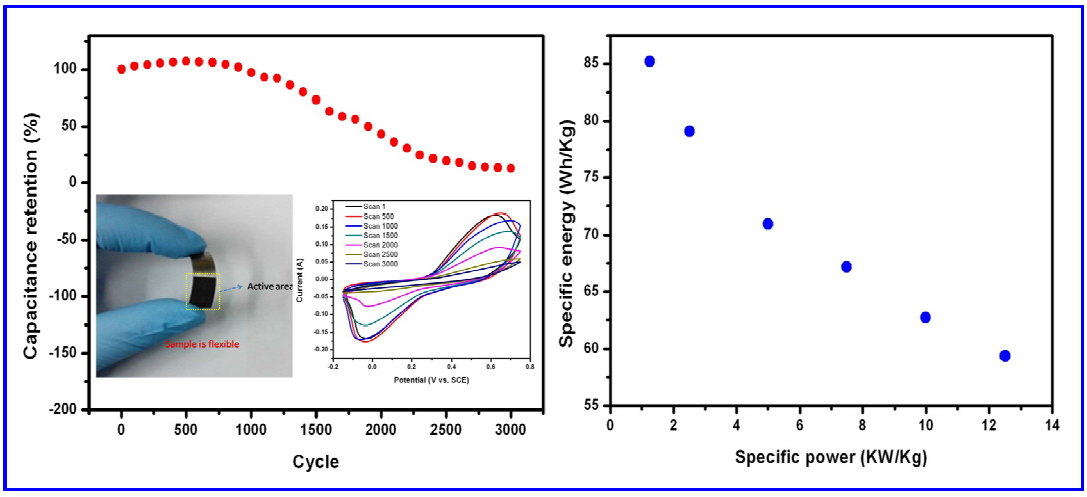

Abstract: A complex hydroxide/metal $Ni(OH)_2$@Ni core-shell electrode was developed for a high-performance and flexible pseudocapacitor. Compared to the conventional $Ni(OH)_2$ electrode, the as-prepared amorphous $Ni(OH)_2$@ three-dimensional (3D)Ni core-shell electrode shows a large specific capacitance of 2868 F g^{-1} at a scan rate of 1 mV s^{-1} and a good cycling stability (3% degradation

after1,000 cycles) at a scan rate of 100 mV s^{-1}. Furthermore, the high rate capability with a specific capacitance of 2454 F g^{-1} can be achieved at a charge/discharge current density of 5 A g^{-1}. An amorphous $Ni(OH)_2$@3D Ni-AC based asymmetric supercapacitor could be cycled reversibly in the high-voltage region between 0-1.3V and the specific capacitance of 92.8 F g^{-1} at 1 A g^{-1}. This research demonstrates that introducing the metal core to conventional hydroxide supercapacitor electrodes could open up new opportunities for designing and developing High-Performance supercapacitors.

Introduction

With the growing concerns about environmental protection and energy crisis in nowadays society, more and more researchers efforts for energy storage and conversion from renewable energy sources.[1-3] , As a promising candidate for energy storage, supercapacitors have attracted much attention in the past decades due to long cycle life, fast charging/discharging rate, and high power density.[4-6] According to the mechanism of charge storage, supercapacitors can be classified into two types: electrochemical double layer capacitors (EDLCs) employing carbon materials[7-9] and pseudocapacitors with conducting polymers[10-12] or transition-metal oxides[13-15] and hydroxides.[16-18] Different to EDLCs, pseudocapacitors can provide much higher capacitance and energy density through fast Faradaic charge transfer reactions. Among various pseudocapacitive materials, $Ni(OH)_2$ has been recognized as a promising electrode material due to its high theoretical specific capacitance. However, they often result in compromises of rate capability and reversibility

because they rely on faradic redox reactions and the active materials are typically too poorly conducting to support fast electron transport required by high rates.[19-20]

To enhance the pseudocapacitor performance of $Ni(OH)_2$, an efficent design is to directly coat $Ni(OH)_2$ onto a high-conductivity current collector, such as two-dimensional (2D) graphene,[21-22] one-dimensional (1D) carbon nanotubes (CNTs),[23-24] or 1D ZnO.[25] Recently, 3D composites have elicited much interest due to their distinctive structural features and intriguing properties.[26-27] In comparison to low-dimensional materials, 3D structures provide a great deal of opportunity to explore their novel properties. Especially, complex metal oxides or hydroxides/metal electrodes with enhanced electrochemical performances in supercapacitors have attracted much interest.[28-30] Worth to be mentioned, electrode materials with amorphous phases are usually evaluated to be unsuitable for electrochemical capacitors because of poor performance.[31] However, Li *et al* recently demonstrated high-performance electrochemical supercapacitors prepared from high-purity amorphous $Ni(OH)_2$ nanospheres synthesized by a simple and green electrochemical process.[32] To the best of our knowledge, up to now, there has been less development in the synthesis of $Ni(OH)_2$/metal composites for supercapacitor applications. Therefore, introducing a Ni core is very promising to improve performance of conventional $Ni(OH)_2$ supercapacitor electrodes.

Herein, we report a simple and effective approach to coat amorphous $Ni(OH)_2$ on Ni metal core. The amorphous $Ni(OH)_2$@Ni core-shell electrode shows an excellent electrochemical performance with a specific capacitance of 1710 F g^{-1} even at a high

charge/discharge rate of 50 A g^{-1}. Furthermore, the amorphous $Ni(OH)_2$@Ni core-shell electrode exhibits excellent cycling stability, and just lost only 3% of their initial capacitance after 1000 cycles at a scan rate of 100 mV s^{-1}. The amorphous $Ni(OH)_2$@Ni core-shell electrode manifests apparent advantages as follows: firstly, amorphous $Ni(OH)_2$@Ni core-shell electrode as 3D array architecture show obvious advantages, such as high aspect ratio, and high interfacial area.[33] Secondly, the amorphous $Ni(OH)_2$ directly grown on 3D-Ni nano particles can provide numerous express pathways for fast electron-transport. Furthermore, electrodeposition process without any binders and carbon black adding, resulting in reduced internal resistance to enhance the rate capability.[34-35] The design idea of this kind of complex hydroxide/metal core-shell nanostuctured configurations could open up new opportunities for the fabrication of high-performance flexible supercapacitors.

Experiment Section

Preparation of 3D nano-Ni particles. All solvents and chemicals were of reagent quality used without further purification. 3D nano-Ni particles were prepared as described by Zhang and coworkers.[36] Before the electrodeposition, Ti (0.5 mm thick, 99.7% purity) foils (1.0 cm × 2.5 cm) were polished mechanically and cleaned with ethanol, acetone and deionized (DI) water by ultrasound for 15 min. The electrodeposition was conducted by a Chenhua CHI 760D model Electrochemical Workstation (Shanghai), with a standard two-electrode glass cell at room temperature, a 1.0 cm × 1.0 cm platinum plate as counter electrode and a piece of Ti foil as the working electrode. The loading area of all samples was defined as 1.0 cm^2

by tape. The electrodeposition of 3D nano-Ni films was performed at a constant current of 0.2 A cm^{-2} for 20 s in a solution of 0.2 M NH_4Cl and 0.01 M $NiCl_2$. After electrodeposition, the samples were taken out and carefully washed with DI water to remove excessive electrolyte and then dried in a vacuum oven at 60 ℃ for 2 h. The loading density of Ni was about 0.67 mg cm^{-2}.

Electrodeposition of amorphous $Ni(OH)_2$@3D-Ni core-shell electrodes. Nickel hydroxide on 3D nano-Ni particles were electrodeposited as the procedure mentioned in earlier report.[37] Electrodeposition of amorphous $Ni(OH)_2$@3D-Ni was carried out in a conventional three-electrode cell using a CHI 760D electrochemical workstation. The working electrode was Ti/3D nano-Ni particles. A 1.0 cm × 1.0 cm platinum plate and a saturated calomel electrode (SCE) served as the counter and reference electrodes, respectively. The deposition condition was performed at a constant potential of -0.7 V in a solution containing 0.1 M $Ni(NO_3)_2$ at room temperature. The electrodeposition time was about 4 min and the $Ni(OH)_2$ film was about 0.5 mg according to Faraday's law. After deposition, the as-prepared $Ni(OH)_2$ electrode was washed with water and ethanol several times.

Preparation of AC negative electrode. 80 wt% of activated carbon, 10 wt% acetylene black and 10 wt% polyvinylidene difluoride (PVDF) binder were mixed in N-methyl-2-pyrrolidone (NMP). The obtained thick paste was coated onto Ti foil (1.0 cm ×1.0 cm). At last, the electrode was dried at 80℃ for 4 h.

Material Characterization The surface morphology and structure of the as-prepared samples were analyzed by using field emission scanning electron microscopy

(FE-SEM, Quanta 400) and transmission electron microscopy (TEM, FEI, Tecnai™ G2F30). Fourier-transform infrared spectroscopy (FT-IR) of the as-prepared products was measured with a Nicolet 5700 spectrometer using KBr sample pellets, laser micro-raman spectrometer (Renishaw Invia) using a visible laser (λ = 514.5 nm) with an output laser power of 50 mW as the excitation wavelength at room temperature. The crystallographic structure of the samples was analyzed using powder X-ray diffraction (XRD, Bruker, D8 ADVANCE) with Kα radiation (*λ* = 1.5418 Å) and transmission electron microscopy (TEM, FEI, Tecnai G2F30). The chemical state and compositions of the products were analyzed using X-ray photoelectron spectroscopy (XPS, ESCALab250).

Electrochemical measurements. Cyclic voltammetry (CV) and galvanostatic charge/discharge (GCD) measurements were conducted using a standard electrode cell with a conventional three-electrode configuration on an electrochemical workstation (CHI 760D). A saturated calomel electrode (SCE) and a Pt plate (1.0 cm × 1.0 cm) were used as reference and counter electrode, respectively. The asymmetric supercapacitor was assembled in a two-electrode configuration using Ti-3D $Ni/Ni(OH)_2$ electrode and Ti-AC as the positive and negative electrodes with one piece of cellulose paper as the separator. All the electrochemical measurements were performed in a 1 M KOH solution at room temperature.

Results and Discussion

A schematic illustration of the procedure used to fabricate the amorphous $Ni(OH)_2$@3D-Ni core-shell electrode is shown in Fig. 1. The homogeneous 3D Ni

nanoparticles are firstly grown on a Ti plate to form the Ni/Ti by a simple electrodeposition process. Fig. 2a shows the low-magnification SEM image of the 3D-nano Ni. It is seen that the as-prepared samples composed of many well-defined nanoparticles. The diameter of the synthesized nanoparticals are approximately 100-200nm (Fig. 2b), and the external surface of the nanoparticals are ravine-like. The $Ni(OH)_2$ layer is also electrodeposited on the Ni/Ti and accordingly the $Ni(OH)_2$@Ni core-shell electrode is fabricated. Fig. 2c and d shows the SEM images of 3D-nano Ni after $Ni(OH)_2$ electrodeposition, suggesting the conformal coating of 3D-nano Ni with $Ni(OH)_2$ film. Fig. 3a shows X-ray diffraction (XRD) pattern of the as-prepared nanostructured composite. All diffraction peaks can be indexed to 3D nano-Ni and Ti substrate, indicating that crystalline Ni was successfully deposited on the Ti substrate. It is worth noting that there is no peak pertaining to $Ni(OH)_2$, which suggests that the deposited $Ni(OH)_2$ is amorphous in nature.[38] The detailed crystal structures were further examined using transmission electron microscopy (TEM). The TEM image in Fig. 3b shows a single $Ni(OH)_2$@3D -Ni core-shell nanoparticle with a diameter of 200-500 nm and a length of 400-800 nm. The TEM, HRTEM and selected-area electron diffraction (SAED) results in Fig. 3b-f reveal that the Ni core is polycrystalline and $Ni(OH)_2$ shell possesses amorphous structure. The inner Ni core shows a polycrystalline structure in Fig.3c and 3e. Moreover, the HRTEM image in Fig. 3f shows a 0.18 nm Ni (200) lattice fringe spacing. The corresponding SAED of $Ni(OH)_2$ shell as shown in Fig. 3d, it is seen that a broad and diffused halo ring , which indicates the $Ni(OH)_2$ shell are amorphous structure. Thus, the TEM results further

confirmed that the $Ni(OH)_2$@3D-Ni composite consisted of a polycrystalline Ni core and an amorphous $Ni(OH)_2$ shell, which is consistent with the XRD results.

In order to identify the structural features of amorphous $Ni(OH)_2$@3D-Ni nanocomposite, we carried out FT-IR and Raman analysis (Fig. 4). Fig. 4a shows IR spectra in the range of 400-4000 cm^{-1}. The peak at 3650 cm^{-1} attributed to the vibration of hydroxyl groups O-H bonded,[39-40] the peaks at 1651 and 1462 cm^{-1} are attributed to the bending vibration of H_2O molecules, the peak at 1362 cm^{-1} can be assigned to the inter-layer NO_3^- anion, and the two peaks around 630 and 480 cm^{-1} are due to the Ni-O stretching vibrations and an in-plane Ni-O-H bending vibration, respectively.[41] The Raman spectrum of the samples shows one broad peak at around 500 cm^{-1} (Fig. 4b), by using a Gaussian fitting method, it can be deconvoluted into two components. The components at 462 and 535cm^{-1} are corresponds to the symmetric Ni-OH stretching mode and vibration of Ni-O stretching , respectively. [42-43]

To gain further information on the chemical composition of the samples, we resort to X-ray photoelectron spectroscopy (XPS) measurement to characterize the sample. The Ni 2p XPS spectrum are shown in Fig. 4c, Two major peaks with binding energies at 855.7 and 873.3 eV, which correspond to Ni $2p_{3/2}$ and Ni $2p_{1/2}$, respectively. The spin-energy separation of 17.6 eV is also the characteristic of a $Ni(OH)_2$ phase. [44-46] The high-resolution spectrum for the O 1s region in Fig. 4d shows three oxygen contributions. The fitted peak at 530.8 eV is typical of metal-oxygen bonds.[47] The peak at 531.5 eV is usually associated with oxygen in OH^-

group.[48-49] Furthermore, the peak at 532.7 eV can be attributed to the multiplicity of physi- and chemisorbed water at or near the surface. [50]

Fig. 5a shows the CV curves of the amorphous $Ni(OH)_2$ @3D-Ni hybrid electrode at scan rates of 1, 2, 5, 10, 20 mV s^{-1} in a potential windows ranging from 0 to 0.5 V (*versus* SCE) in 1 M KOH aqueous solution. All of those curves include two strong redox peaks, not an ideal rectangular shape, indicating that the capacitance characteristics are mainly due to pseudocapacitive processes, which are based on a redox mechanism. The surface Faradaic reactions of the $Ni(OH)_2$ electrode materials can be expressed as [46]

$$Ni(OH)_2 + OH^- \longleftrightarrow NiOOH + H_2O + e^- \quad (1)$$

The anodic oxidation peak in the range of 0.3-0.5 V and the reduction peak at 0-0.3 V are associated with the reversible reactions of $Ni(OH)_2$/NiOOH. The symmetry of the CV curves is significantly distorted as the scan rate increases and the asymmetrical nature of the anodic and respective cathodic peak at high scan rate is due to kinetic irreversibility of the redox process.[46] The specific capacitance (C_{sp})was calculated from the area under the CV curve [37-38, 46-47]

$$C_{sp} = \frac{1}{mv(V_c - V_a)} \int_{V_a}^{V_c} I(V)dV \quad (2)$$

Where *m* is the mass of the electrode active materials in the electrodes (g), *v* is the potential scan rate (mV s^{-1}), V_c-V_a is the potential range, *I* (V) is the response current (A). The specific capacitance of 3D $Ni(OH)_2$@Ni core-shell hybrid (based on the mass of pristine $Ni(OH)_2$) was summarized in Fig. 5b, which is 2868, 2857, 2587, and 1980 F g^{-1} at scan rates of 1, 2, 5, 10 mV s^{-1}, respectively. The specific capacitances are

higher than of bare $Ni(OH)_2$ and many other $Ni(OH)_2$ composite electrodes, such as Graphene/$Ni(OH)_2$nanoplates (~1267 F g^{-1}) at ascan rate of 5 mV s^{-1},[21] $Ni(OH)_2$/MWCNT composites (~1487 F g^{-1}) at a scan rate of 5 mV s^{-1}.[24] To eliminate the extra capacitance in the electrochemical measurements, CV curves of pure 3D nano-Ni electrode were measured under similar conditions (Fig. 5c-d). At the scan rate of 1 mV s^{-1}, the specific capacitance of the amorphous $Ni(OH)_2$@3D-Ni electrode can achieve 2868 F g^{-1} (based on the mass of pristine $Ni(OH)_2$), while that of the 3D nano-Ni/Ti composites electrode is only 46.6 F g^{-1}. Therefore, in the amorphous $Ni(OH)_2$@3D-Ni electrode, the capacitances contributed by the 3D nano-Ni which served as a current collector was negligible.

Rate capability is one of the important factors for evaluating the power applications of supercapacitors. Fig. 6a shows GCD curves at various current densities ranging from 5 to 50 A g^{-1}. The specific capacitances of the amorphous $Ni(OH)_2$@3D-Ni electrode derived from GV curves can be according to: [21, 24, 26, 38]

$$C_{sp} = \frac{Idt}{mdV} \qquad (3)$$

where C_{sp} (F g^{-1}) is the specific capacitance, m (g) is the mass of Ni(OH) and dV is the potential range, I (A) is the discharge current, dt (s) is the time of discharge process. Fig . 6b shows the specific capacitances of the amorphous $Ni(OH)_2$@3D-Ni electrode at different charge/discharge rates (current densities). The specific capacitances were obtained as 2454, 2278, 2044, 1938, 1808 and 1710 F g^{-1} at current densities of 5 (I = 0.0025 A), 10 (I = 0.005 A), 20 (I = 0.01 A), 30 (I = 0.015 A), 40 (I = 0.02 A) and 50 (I = 0.025 A) A g^{-1}, respectively. The specific capacitance of the amorphous

$Ni(OH)_2$@3D-Ni electrode gradually decreases with increasing current density. 70% of capacitance is maintained when the charge/discharge rate changes from 5 A g^{-1} to 50 A g^{-1}. The value of specific capacitance obtained by the charge/discharge and CV technique are comparable. Besides, these values are much higher than of bare $Ni(OH)_2$ electrodes (1868 F g^{-1} at 20 A g^{-1}).[38] We also measured the charge-discharge curves of the 3D nano-Ni electrode at various current densities (Fig. 6c-d), the current densities of 1, 2, and 5 A g^{-1} correspond to current with 0.001, 0.002, and 0.005 A. The discharge time of bare nano-Ni film is only a few seconds at high-rate charge/discharge, so we can neglect the capacitance of the bare nano-Ni when we calculated the specific capacitance of amorphous $Ni(OH)_2$ @3D-Ni electrode in this case.

Fig. 7a shows the capacitance retention of the amorphous $Ni(OH)_2$ @3D-Ni electrode as a function of cycle number at a scan rate of 100 mV s^{-1}, resulting in a noticeable discharge specific capacitance loss (about 70% after 3000 cycles), which can be mainly attributed to amorphous $Ni(OH)_2$ @3D Ni composite flaking off from Ti foils substrate. However, it is significant that the capacitance is lost only 3% after 1000 cycles. Therefore, the deposited amorphous $Ni(OH)_2$@3D-Ni core-shell composite electrode shows the satisfactory electrochemical stability for long-term and high specific capacitance capacitor applications. Specific energy, $E = (CU_0^2/2)$, and specific power, $P = (E/t)$ are two key factors for evaluating the power applications of electrochemical supercapacitors. Where U_0 is the potential range (V) and t is the time of discharge process (s). A good electrochemical supercapacitor is

expected to provide high energy density or high specific capacitance at high charging/discharging rates (current densities).[51] Fig. 7b shows the Ragone plot of the amorphous $Ni(OH)_2$ @3D-Ni electrode calculated from GCD curves at the different current densities in 1 M KOH aqueous solution. For amorphous $Ni(OH)_2$ @3D-Ni, the specific energy decreases, while the specific power increases as the current increased from 5 to 50 A g^{-1}. It could deliver a high energy desity of 59.3 Wh kg^{-1} even at a high power density of 12.5 kW kg^{-1}. These values are much higher than those of conventional supercapacitors [52]

To further evaluate the capacitive performance of amorphous $Ni(OH)_2$@3D Ni-Ti electrode electrode for practical application, an amorphous $Ni(OH)_2$@3D Ni-AC based asymmetric capacitor was fabricated in this work. Fig 8a shows the CV curves of the $Ni(OH)_2$ @3D Ni electrode and the AC electrode in a three-electrode cell at a scan rate 5 mV s^{-1}. The specific capacitances of $Ni(OH)_2$ @3D Ni-Ti electrode (based on the total mass of $Ni(OH)_2$@3D Ni) and AC electrode were calculated to be 1105 F g^{-1} and 122.6 F g^{-1} at scan rates of 5 mV s^{-1}, respectively. Since the two electrodes have different specific capacitance, in order to obtain a well electrochemical performance for supercapacitor, the charge balance between the two electrodes should be follow the relationship of $q_+ = q_-$, where q_+ and q_- mean the charges stored at positive and negative electrode, respectively. The q is calculated by the equation of $q = C \times \Delta E \times m$. Thus, the mass ratio between the two electrodes is given by the equation:

$$\frac{m_+}{m_-} = \frac{C_- \cdot \Delta E_-}{C_+ \cdot \Delta E_+} \qquad (4)$$

where *C* is the specific capacitance, *ΔE* is the potential range for the charge/discharge process. Hence, the mass ratio between positive and negative electrodes of the $Ni(OH)_2$ @3D Ni-AC based asymmetric capacitor should be 5.63. The total mass of the active materials on the anode was 1.17 mg cm^{-2}, and that of on the cathode was 6.6 mg cm^{-2}. Fig 8b show the CV cures of the $Ni(OH)_2$@3D Ni-AC based asymmetric capacitor at various scan rates between 0.0 and 1.3 V. Each curve exhibited a large current area with broad redox peak, which was the characteristic of the electric double layer capacitance and Faradaic pseudocapacitance. GCD measurements were made at various current densities as presented in Fig. 8c. Fig 8d shows the calculated specific capacitances of the $Ni(OH)_2$ @3D Ni-AC based asymmetric capacitor at various current density. Based on the total mass of the active materials of the two electrodes, the specific capacitances of 92.8, 64.5, 50, 39, 33F g^{-1} were obtained at the current densities of 1, 2, 5, 8, 10A g^{-1}, respectively. The specific capacitance of the device is limited by that of the AC-negative electrode.

Long cycle stability is another critical requirement for practical applications of supercapacitors. The cycling life test over 3000 cycles for the $Ni(OH)_2$@3D Ni-AC based asymmetric capacitor was measured at a scan rate of 200 mV s^{-1} between 0 and 1.3 V. Fig. 9a exhibits the excellent long-term cycling stability of the asymmetric supercapacitor device. The specific capacitance can still retain 96 % of the initial capacitance after 3000 cycles cycling. Fig. 9b shows the Ragone plot of the amorphous $Ni(OH)_2$ @3D Ni-AC based asymmetric capacitor electrode calculated from GCD curves at the different current densities. Our asymmetric capacitor has

achieved an Specific energy of 21.8Wh kg^{-1},as a specific power of 0.66 kW kg^{-1}, the energy density is higher than those of many solid-state supercapacitors.[52]

Conclusion

In summary, we have successfully fabricated a novel hydroxide/metal amorphous $Ni(OH)_2$@3D-Ni core-shell electrode with 3D surface for supercapacitor application via a simple and green two-step electrochemical method. Compared to the conventional $Ni(OH)_2$ electrode, the 3D $Ni(OH)_2$@Ni core-shell electrode exhibited an significant enhancement of supercapacitor performance with a C_{sp} value of 2848 F g^{-1} at 1 mV s^{-1}. High electrochemical stability was also observed, over 1000 cycles without obvious decrease in C_{sp}. An asymmetric supercapacitor based on amorphous $Ni(OH)_2$@3D Ni-AC in aqueous electrolyte had high power density with moderate energy density in a fully packaged device. This work demonstrates that introducing a metal core can effectively improve the supercapacitor performance of the conventional hydroxide electrode. It could open up new opportunities for developing high-performance flexible supercapacitors.

Acknowledgements

The authors acknowledge the financial support of this work by Natural Science Foundations of China (Grant No. 21306030), the Natural Science Foundations of Guangdong Province(Grant No. s2012010009719 and s2013040015229), the Innovative Talents Cultivation Project of Guangdong Province (Grant No. LYM11096), the Science and Technology Project of Guangzhou (Grant No. 12C52011621 and 12C52011624), Scientific Research Project of Guangzhou Municipal Colleges and

Universities (Grant No. 2012A064), and the Fresh Talent Program of Guangzhou University (Grant No. 201302).

Notes and references

[1] J. R. Miller, P. Simon, *Science,* 2008, **321**, 651-652.

[2] G. P. Wang, L. Zhang, J. J. Zhang, *Chem. Soc. Rev*., 2012, **41**, 797-828.

[3] S. Chen, S. Z. Qiao, *ACS Nano,* 2013, **7**, 10190-10196.

[4] X. H. Lu, D. Z. Zheng, T. Zhai, Z. Q. Liu, Y. Y. Huang, S. Xie, Y. X. Tong, *Energy Environ. Sci*., 2011, **4**, 2915-2921.

[5] Q. Li, Z. L. Wang, G. R. Li, R. Guo, L. X. Ding, Y. X. Tong, *Nano Lett*., 2012, **12**, 3803-3807.

[6] M. F. El-Kady, V. Strong, S. Dubin, R. B. Kaner, *Science,* 2012, **335**, 1326-1330.

[7] P. J. Hall, M. Mirzaeian, S. I. Fletcher, F. B. Sillars, A. J. R. Rennie, G. O. Shitta-Bey, G. Wilson, A. Cruden, R. Carter, *Energy Environ. Sci*., 2010, **3**, 1238-1251.

[8] L. L. Zhang, X. S. Zhao, *Chem. Soc. Rev*., 2009, **38**, 2520-2531.

[9] C. Liu, F. Li, L. P. Ma, H. M. Cheng, *Adv. Mater*., 2010, **22**, E28-E62.

[10] K. L. Zhang, L. Zhang, X. S. Zhao, J. Wu, *Chem. Mater*., 2010, **22**, 1392-1401.

[11] Z. L. Wang, R. Guo, G. R. Li, H. H. Lu, Z. Q. Liu, F.M. Xiao, M. Zhang, Y. X. Tong, *J. Mater. Chem*., 2012, **22**, 2401-2404.

[12] Y. Zhao, B. R. Liu, L. J. Pan, G. H. Yu, *Energy Environ. Sci*., 2013, **6**, 2856-2870.

[13] T. Brezesinski, J. Wang, S. Tolbert, B. Dunn, *Nat. Mater*., 2010, **9**, 146-151.

[14] J. Jiang, Y. Y. Li, J. P. Liu, X. T. Huang, C. Z. Yuan, X. W. Lou, *Adv. Mater*., 2012, **24**, 5166-5180.

[15] X. Sun, Q. Li, Y. N. Lü, Y. B. Mao, *Chem. Commun*., 2013, **49**, 4456-4458.

[16] R. R. Salunkhe, B. P. Bastakoti, C. T. Hsu, N. Suzuki, J. H. Kim, S. X. Dou, C. C. Hu, Y. Yamauchi, *Chem. Eur. J*., 2014, **20**, 3084-3088.

[17] C. Guan, J. P. Liu, C. W. Cheng, H. X. Li, X. L. Li, W. W. Zhou, H. Zhang, H. J. Fan, *Energy Environ. Sci*., 2011, **4**, 4496-4499.

[18] C. Q. Shang, S. Dong, S. M. Wang, D. D. Xiao, P. X. Han, X. G. Wang, L. Gu, G. L. Cui, *ACS Nano,* 2013, **7**, 5430-5436.

[19] J. Li, F. L. Luo, X. Q. Tian, Y. Lei, H. Y. Yuan, D. Xiao, *J. Power Sources,* 2013, **243**, 721-727.

[20] G. S. Gund, D. P. Dubal, S. B. Jambure, S. S. Shinde, C. D. Lokhande, *J. Mater. Chem. A,* 2013, **1**, 4793-4803.

[21] H. L. Wang, H. S. Casalongue, Y. Y. Liang, H. J. Dai, *J. Am. Chem. Soc*., 2010, **132**, 7472-7477.

[22] S. Chen, J. J. Duan, Y. H. Tang, S. Z. Qiao, *Chem. Eur. J*., 2013, **19**, 7118-7124.

[23] M. Shahid, J. Liu, I. Shakir, M. F. Warsi, M. Nadeem, Y. U. Kwon, *Electrochim. Acta,* 2012, **85**, 243-247.

[24] D. P. Dubal, G. S. Gund, C. D. Lokhande, R. Holze, *ACS Appl. Mater. Interfaces,* 2013, **5**, 2446-2454.

[25] Z. Pu, Q. Liu, A. H. Qusti, A. M. Asiri, A. O. Al-Youbi, X. P. Sun, *Electrochim. Acta,* 2013, **109**, 252-255.

[26] Y. Wang, S. L. Gai, N. Niu, F. He, P. P. Yang, *J. Mater. Chem. A,* 2013, **1**, 9083-9091.

[27] J. Y. Ji, L. L. Zhang, H. X. Ji, Y. Li, X. Zhao, X. Bai, X. B. Fan, F. B. Zhang, R. S. Ruoff, *ACS Nano,* 2013, **7**, 6237-6243.

[28] X. H. Xia, J. P. Tu, Y. Q. Zhang, Y. J. Mai, X. L. Wang, C. D. Gu, X. B. Zhao, *J. Phys. Chem. C,* 2011, **115**, 22662-22668.

[29] X. Q. Meng, M. Zhou, X. L. Li, J. Y. Yao, J. Li, F. L. Liu, H. C. He, P. Xiao, Y. H. Zhang, *Electrochim. Acta,* 2013, **109**, 20-26.

[30] H. Pang, S. M. Wang, G. C. Li, Y. H. Ma, J. Li, X. X. Li, L. Zhang, J. S. Zhang, H. H. Zheng, *J. Mater. Chem. A.,* 2013, **1**, 5053-5060.

[31] C. C. Hu, J. C. Chen, K. H. Chang, *J. Power. Sources,* 2013, **221**, 128-133.

[32] H. B. Li, M. H. Yu, F. X. Wang, Y. Liang, J. Xiao, C. X. Wang, Y. X. Tong, W. Yang, *Nat. Commun*., 2013, **4**, 1894.

[33] Y. Lei, J. Li, Y. Y. Wang, L. Gu, Y. F. Chang, H. Y. Yuan, D. Xiao, *ACS Appl. Mater. Interfaces,* 2014, **6**, 1773-1780.

[34] D. Guo, H. M. Zhang, X. Z. Yu, M. Zhang, P. Zhang, Q. H. Li, T. H. Wang, *J. Mater. Chem. A,* 2013, **1**, 7247-7254.

[35] D. N. Lei, M. H. Zhang, B. H. Qu, L. B. Chen, Y. G. Wang, E. D. Zhang, Z. Xu, Q.H. Li, T. H. Wang, *Nanoscale,* 2012, **4**, 3422-3426.

[36] Y. Q. Zhang, X. H. Xia, X. L. Wang, Y. J. Mai, S. J. Shi, Y. Y. Tang, C. G. Gu, J. P. Tu, *J. Power Sources,* 2012, **213**, 106-111.

[37] G. W. Yang, C. L. Xu, H. L. Li, *Chem. Commun*., 2008, 6537-6539.

[38] H. B. Li, M. H. Yu, X. H. Lu, P. Liu, Y. Liang, J. Xiao, Y. X. Tong, G. W. Yang, *ACS Appl. Mater. Interfaces,* 2014, **6**, 745-749.

[39] P. Hermet, L. Gourrier, J. L. Bantignies, D. Ravot, T. Michel, S. Deabate, P. Boulet, F. Henn, *Phys. Rev. B,* 2011, **84**, 235211.

[40] J. L. Bantignies, S. Deabate, A. Righi, S. Rols, P. Hermet, J. L. Sauvajol, F. Henn, *J. Phys. Chem. C.,* 2008, **112**, 2193-2201.

[41] S. J. Kim, G. J. Park, B. C. Kim, J. K. Chung, G. G. Wallacec, S. Y. Park, *Synth. Met*., 2012, **161**, 2641-2646.

[42] H. Miyamoto, *Mater. Res. Bull*., 1976, **11**, 599-607.

[43] S. D. Tiwari, K. P. Rajeev, *Phys. Rev. B,* 2008, **77**, 224430.

[44] M. C. Biesinger, L. W. M. Lau, A. R. Gersonb, R. S. C. Smart, *Phys. Chem. Chem. Phys*., 2012, **14**, 2434-2442.

[45] J. Yan, Z. J. Fan, W. Sun, G. Q. Ning, T. Wei, Q. Zhang, R. F. Zhang, L. J. Zhi, F. Wei, *Adv. Funct. Mater*., 2012, **22**, 2632-2641.

[46] J. W. Lee, T. Ahn, D. Soundararajan, J. M. Koc, J. Kim, *Chem. Commun*., 2011, **47**, 6305-6307.

[47] Z. Q. Liu, K. Xiao, Q. Z. Xu, N. Li, Y. Z. Su, H. J. Wang, S. Chen, *RSC Adv*., 2013, **4**, 4372-4380.

[48] B. P. Payne, M. C. Biesinger, N. S. McIntyrea, *J. Electron. Spectrosc*., 2012, **185**, 159-166.

[49] C. M. Zhao, X. Wang, S. M. Wang, Y. Y. Wang, Y. X. Zhao, W. T. Zheng, *Int. J. Hydrogen Energy,* 2012, **37**, 11846-11852.

[50] Z. Q. Liu, Q. Z. Xu, J. Y. Wang, N. Li, S. H. Guo, Y. Z. Su, H. J. Wang, J. H. Zhang, S. Chen, *Int. J. Hydrogen Energy,* 2013, **38**, 6657-6662.

[51] L. H. Bao, J. F. Zang, X. D. Li, *Nano Lett.,* 2011, **11,** 1215-1220.

[52] Y. Gogotsi, P. Simon, *Science,* 2011, **334**, 917-918.

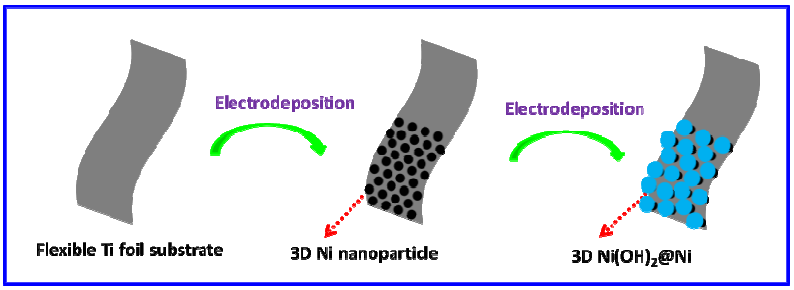

Fig. 1 Schematic illustration for the fabrication of $Ni(OH)_2$ @ 3D Ni core-shell composite.

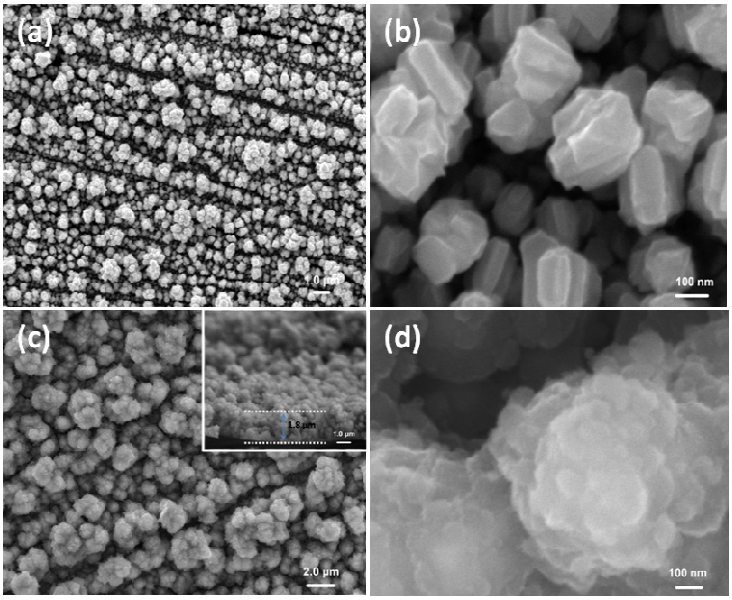

Fig. 2 (a-b) SEM images of the 3D nano-Ni particles; (c-d) $Ni(OH)_2$@ 3D Nicore-shell composite and the inset is the cross section image.

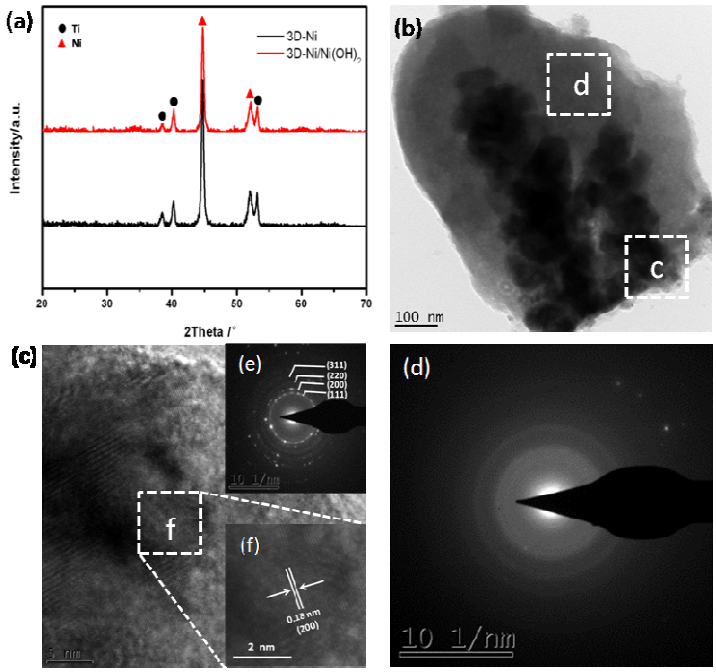

Fig. 3 (a) XRD patterns of 3D-nano Ni, and $Ni(OH)_2$ @3D Ni core-shell composite; (b-f) TEM image, HRTEM image and the corresponding SAED pattern of $Ni(OH)_2$ @ 3D Ni core-shell composite.

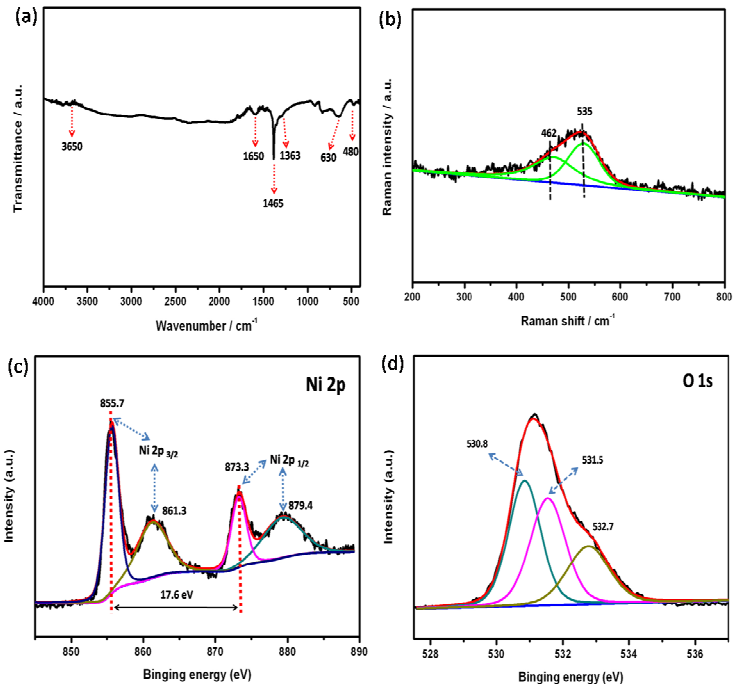

Fig. 4 (a-b) IR and Raman spectrum of the $Ni(OH)_2$ @3D Ni core-shell composite; (c-d) XPS spectrum of $Ni(OH)_2$ @3D Ni core-shell composite with the high-resolution spectra of Ni 2p and O 1s, respectively.

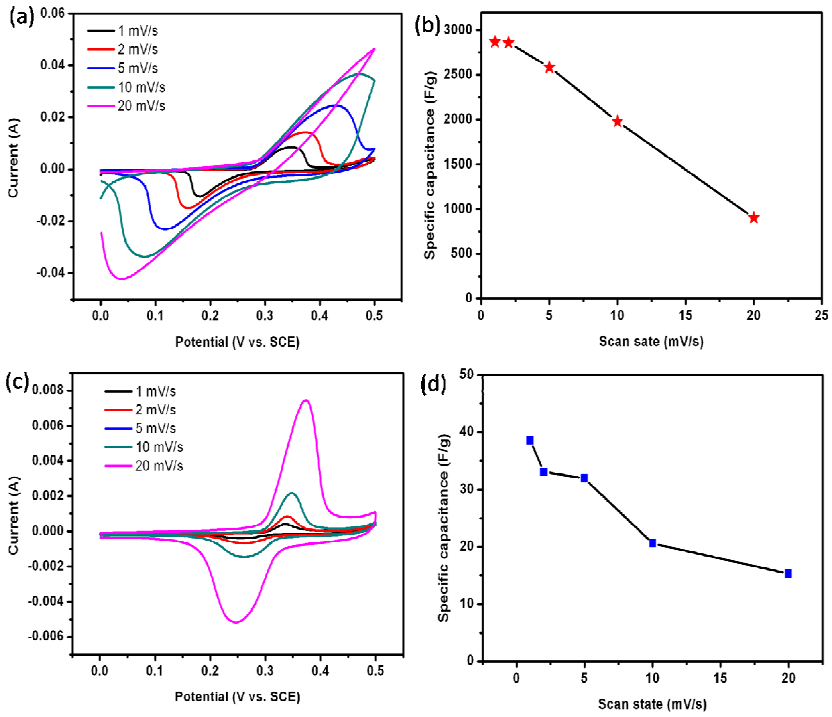

Fig. 5 (a) CV curves of the $Ni(OH)_2$ @ 3D Ni core-shell electrode at various scan rates in 1M KOH; (b) Specific capacitance of the $Ni(OH)_2$ @ 3D Ni core-shell electrode as a function of the scan rates based on the CV curves; (c) CV curves of the 3D nano-Ni electrode at various scan rates in 1M KOH; (d) Specific capacitance of the 3D nano-Ni electrode as a function of the scan rates based on the CV curves.

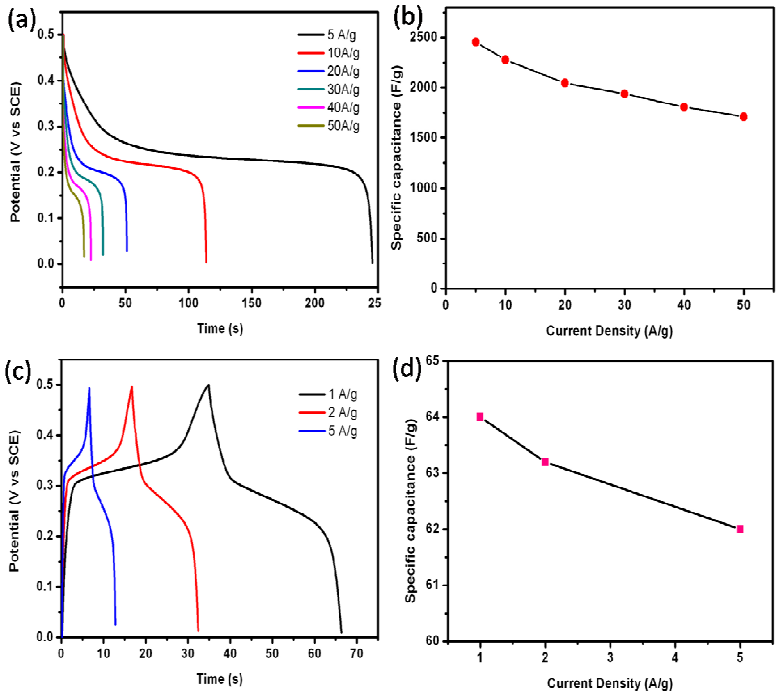

Fig. 6 (a) Discharge curves of amorphous $Ni(OH)_2$ @3D Ni core-shell electrode at various current densities; (b) Specific capacitance of amorphous $Ni(OH)_2$ @3D Ni core-shell electrode at various discharge current densities; (c) Charge-discharge curves of 3D nano-Ni electrode at various current densities; (d) Specific capacitance of 3D nano-Ni at various discharge current densities.

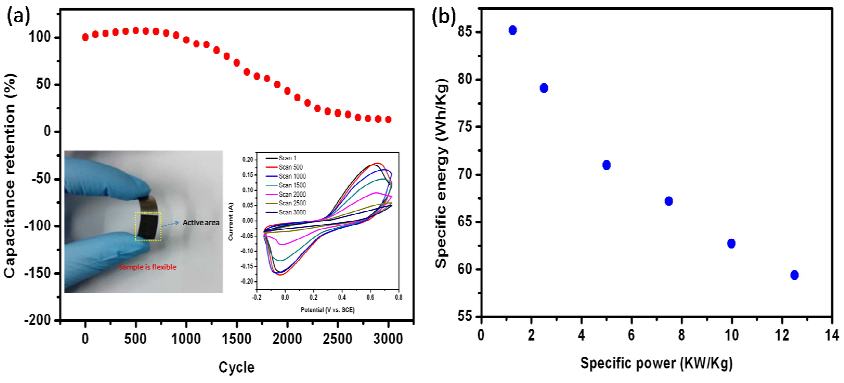

Fig. 7 (a) Variation of the specific capacitance of amorphous $Ni(OH)_2$ @3D Ni

electrodes as a function of cycle number measured at 100 mV s^{-1} in 1 M KOH electrolyte (the left of inset is a photo image of the flexible electrode, the right of inset is the CV curves of the 1st, 500th, 1000th, 1500th, 2000th, 2500th, and 3000th cycles); (b) Ragone plot of the estimated specific energy and specific power at various charge/discharge rates (5, 10, 20, 30, 40, 50 A g^{-1}).

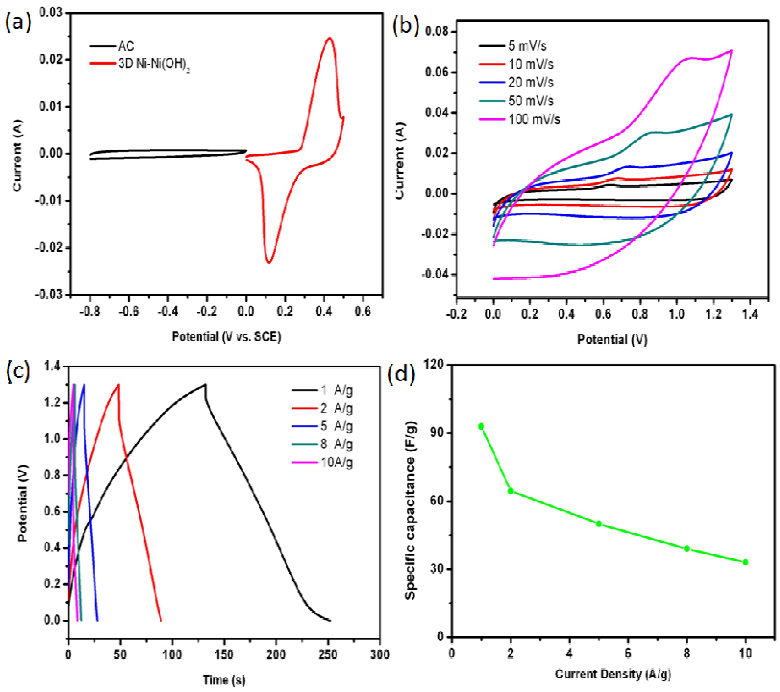

Fig. 8 (a) Comparative CV curves of AC and amorphous $Ni(OH)_2$ @3D Ni electrodes at a scan rate of 5 mV s^{-1}; (b) CV curves of amorphous $Ni(OH)_2$ @3D Ni-AC based asymmetric capacitor at various scan rates; (c) The charge/discharge curves of amorphous $Ni(OH)_2$ @3D Ni-AC based asymmetric capacitor at different current densities; (d) calculated specific capacitance as a function of current density.

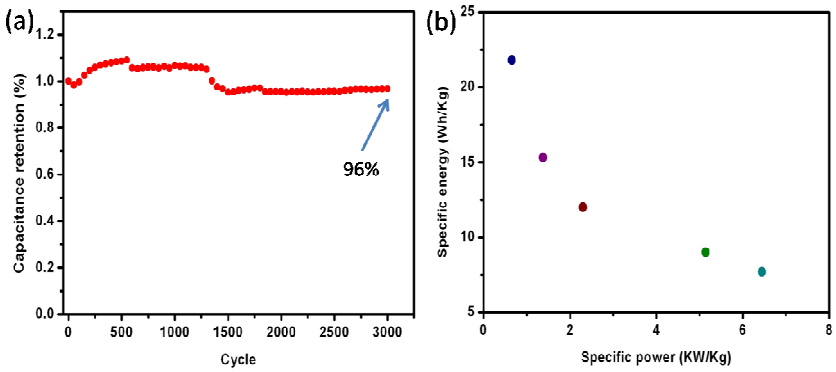

Fig. 9 (a) Variation of the specific capacitance of amorphous $Ni(OH)_2$ @3D Ni-AC based asymmetric capacitor as a function of cycle number measured at 200 mV s^{-1} in 1 M KOH electrolyte; (b) Ragone plot of the estimated specific energy and specific power at various charge/discharge rates (1, 2, 5, 8, 10 A g^{-1}).